

Imaging magnetism evolution of magnetite to megabar pressure range with quantum sensors in diamond anvil cell

Authors:

Mengqi Wang^{1,3,†}, Yu Wang^{2,6,†*}, Zhixian Liu^{1,3,†}, Ganyu Xu^{1,3}, Bo Yang^{1,3}, Pei Yu^{1,3}, Haoyu Sun^{1,3}, Xiangyu Ye^{1,3}, Jingwei Zhou^{1,3}, Alexander. F. Goncharov⁷, Ya Wang^{1,3,4*} and Jiangfeng Du^{1,3,4,5*}

Affiliations:

¹ CAS Key Laboratory of Microscale Magnetic Resonance and School of Physical Sciences, University of Science and Technology of China, Hefei 230026, China

² Key Laboratory of Materials Physics, Institute of Solid State Physics, HFIPS, Chinese Academy of Sciences, Hefei, China.

³ CAS Center for Excellence in Quantum Information and Quantum Physics, University of Science and Technology of China, Hefei 230026, China

⁴ Hefei National Laboratory, University of Science and Technology of China, Hefei 230088, China

⁵ Institute of Quantum Sensing and School of Physics, Zhejiang University, Hangzhou 310027, China

⁶ Institute of Geosciences, Goethe University Frankfurt, Frankfurt 60438, Germany

⁷ Earth and Planets Laboratory, Carnegie Institution of Washington, Washington, DC, USA.

*Corresponding author. Email: wangyu@issp.ac.cn (Yu Wang), ywustc@ustc.edu.cn (Ya Wang) and djf@ustc.edu.cn (Jiangfeng Du)

†These authors contributed equally to this work

Abstract

High-pressure diamond anvil cells have been widely used to create novel states of matter. Nevertheless, the lack of universal in-situ magnetic measurement techniques at megabar pressures makes it difficult to understand the underlying physics of materials' behavior at extreme conditions, such as high-temperature superconductivity of hydrides and the formation or destruction of the local magnetic moments in magnetic systems, etc. Here we break through the limitations of pressure on quantum sensors and develop the in-situ magnetic detection technique at megabar pressures with high sensitivity

($\sim 1 \mu\text{T}/\sqrt{\text{Hz}}$) and sub-microscale spatial resolution. By directly imaging the magnetic field and the evolution of magnetic domains, we observe the macroscopic magnetic transition of Fe_3O_4 in the megabar pressure range from strong ferromagnetism ($\alpha\text{-Fe}_3\text{O}_4$) to weak ferromagnetism ($\beta\text{-Fe}_3\text{O}_4$) and finally to non-magnetism ($\gamma\text{-Fe}_3\text{O}_4$). The scenarios for magnetic changes in Fe_3O_4 characterized here shed light on the direct magnetic microstructure observation in bulk materials at high pressure and contribute to understanding the mechanism of magnetic moment suppression related to spin crossover. The presented method can potentially investigate the spin-orbital coupling and magnetism-superconductivity competition in magnetic systems.

Introduction

Pressure has been proved to be powerful tools to tune the magnetic properties of materials as it can effectively increase the intermolecular interaction and redistribute the electrons¹⁻³. For example, the spin crossover in 3d transition metal compounds depicted by the competition of the spin exchange and crystal field energy on compression⁴, and the effect of covalency of the neighbored metal ions⁵.

Additionally, measurements of magnetic properties at high pressures are extremely instrumental in high T_c superconducting materials such as polyhydrides, where there is a high controversy about their existence and properties⁶⁻⁸ due to a lack of sufficient evidence of the Meissner effect. Many efforts have been made to adapt magnetic detection methods to Diamond Anvil Cell (DAC) facilities. High energy photon/neutron scattering techniques such as x-ray magnetic circular dichroism (XMCD), Neutron magnetic scattering, and Mössbauer spectroscopy are widely used for magnetic measurements in DACs^{9,10}. These techniques are able to probe atomic-scale magnetism and resolve local element-specific magnetism issues. However, these methods are not sensitive to magnetic phenomena like Meissner effect and technically restricted by sample and beam size at high pressure, and the quantitative analysis remains challenging on account of the resolution limited spectra¹¹. The magnetization of the materials can be directly measured by integrating DAC into superconducting quantum interference devices (SQUID), but the effect of the DAC apparatus' background cannot be separated from the magnetization of the micrometer-scale samples, resulting in the lack of spatial resolution and the disadvantage to detect the magnetization of inhomogeneous sample synthesized at high pressure and high temperature inside the high-pressure chamber^{12,13}.

In recent years, NV centers in diamond have been proposed as quantum sensors for new type of high-pressure magnetic measurements, as they can be set in nanoscales to the sample inside the pressure chamber to detect the complex free-space magnetic field textures generated by high-pressure samples and able to provide significant potential advantages in terms of sensitivity and spatial resolution¹⁴⁻¹⁶. However, NV centers' magnetic sensing capabilities associated with their optical and spin properties could be dramatically degraded by the surrounding stress environment. Recent works show that in complex stress environment both the optical-spin readout contrast worsen and spin resonance linewidth becomes broader leading to a sharp drop in sensitivity as the pressure approaches megabar level^{17,18}. Understanding the stress-induced effect and maintaining excellent performances of NV centers present substantial challenges for applying this technique to reveal the magnetically related physics above megabar pressures.

In this work, we explore the impact of stress on the optical and spin properties of NV centers. Then by modulating the uniaxial stress along nitrogen-vacancy axis, we improve the magnetic detective sensitivity to $\sim 1 \mu\text{T}/\sqrt{\text{Hz}}$ at 130 GPa, which is promising for nano-scale single-domain grain detection^{19,20}. Based on the sensitivity of the NV quantum sensors achieved, we investigated the magnetism change of the Fe_3O_4 – one of the oldest magnetic mineral on the earth²¹ – at pressures well exceeding a megabar at room temperature.

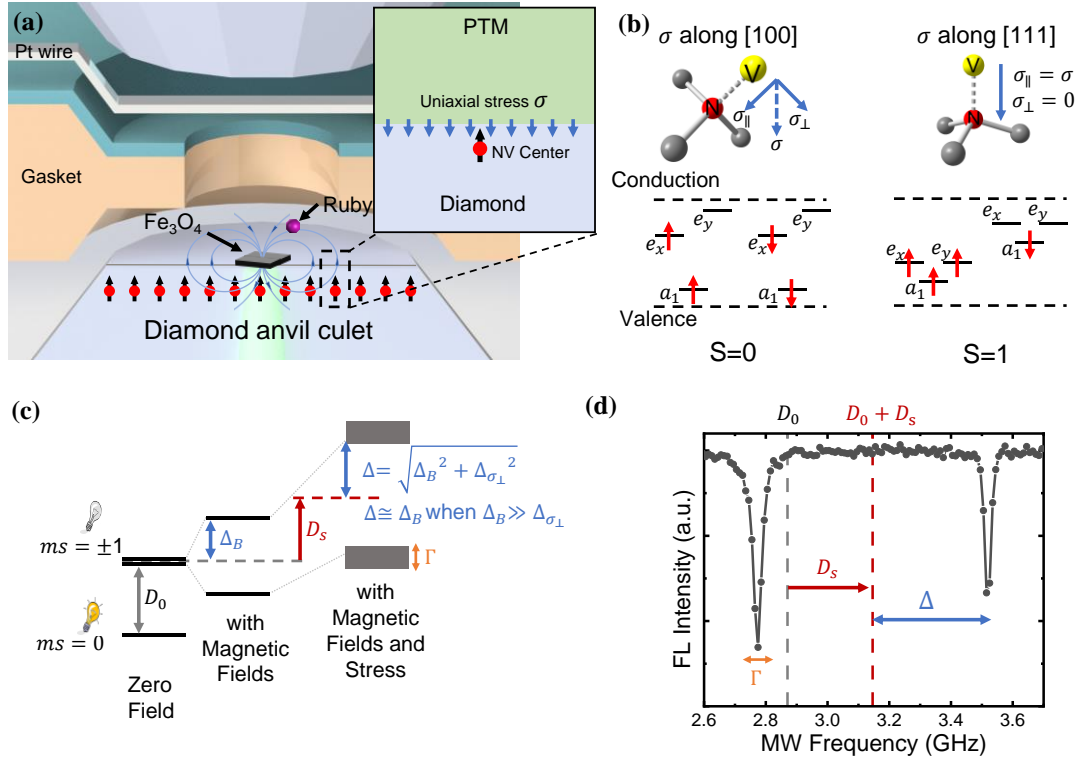


Figure 1. Schematic geometry NV centers in the DAC. (a) Schematic of the DAC geometry. The shallow layer of NV centers is embedded in the diamond anvil culet and a single crystal of Fe_3O_4 is placed on the surface of the same culet. The 532 nm laser is used to optically initialize and read out the spin state of NV centers. The Pt wire is used to transfer the microwave for controlling the spin state. Ruby fluorescence and diamond edge Raman are used to calibrate pressures in DAC chamber. The inset shows the uniaxial stress component σ perpendicular to the surface of culet. (b) The electronic ground state levels of the NV center under megabar uniaxial stress by first-principles calculations. Left: uniaxial stress applied to the [100] crystal direction. Right: uniaxial stress applied to the [111] crystal direction. (c) The spin ground state energy structure of the NV^- and the evolution with the existence of both magnetic field and stress environment. The fluorescence intensity of the NV center is dependent on the spin states ($ms=0$, bright; $ms = \pm 1$, dark). And the spin states can be initialized to $ms=0$ by laser and coherently manipulated by microwave. $D_0 = 2.87$ GHz is the zero-field splitting. Δ_B is half of the Zeeman splitting energy with external magnetic field. D_s is the energy shift of the zero-field splitting caused by the axial stress component. $\Delta_{\sigma_{\perp}}$ is half of the splitting in $ms = \pm 1$ spin sublevels produced by the shear stress in NV's frame. Γ is the additional broadening of the sublevels for the ensemble NV centers in inhomogeneous stress. (d) The corresponding optically detected magnetic resonance (ODMR) spectrum at 46.3 GPa presenting the spin states in (c). The dashed grey line marks the peak position (D_0) at ambient conditions with no magnetic field, and the dashed red line marks the central position ($D_0 + D_s$) of two separated peaks at high pressure with a parallel magnetic field (~ 133 Gs). The data extraction of D_0 , D_s , Δ , and Γ allow to determine the magnitude of the stress and external magnetic fields.

Results

Quantum sensors at megabar pressures.

Firstly, to understand the impact of the stress on the sensors, we investigated the electronic energy level of the NV center under uniaxial stress with different directions by first-principles calculations (Fig. 1b). The stress component σ_{\perp} perpendicular to the NV axis breaks the C_{3V} symmetry, leading to a ground spin state transition of NV from triplet state ($S=1$) to single state ($S=0$) and ultimately resulting in a loss of magnetic detection ability. However, the stress applied along the NV axis preserves the spin property of NV centers, enabling high-pressure magnetic measurements. At the anvil tip, the stress comprises both hydrostatic pressure (ρ) and uniaxial stress (σ) perpendicular to the surface²², allowing for modulation of uniaxial stress direction on NV centers through control of anvil crystal orientation. For NV centers oriented along [111] direction in the (111)-cut anvil, the component σ_{\perp} can be minimized. As a result, the contrast between $ms=0$ and $ms = \pm 1$ in the ODMR spectrum remains high as pressure increases to megabar range (Fig. 2a). Notably, at 130 GPa, we observed a contrast enhancement of $\sim 30\%$, much higher than that at 1.5 GPa (Fig. 2f). This suggests that NV centers oriented in the other three crystallographically equivalent directions ($[\bar{1}\bar{1}\bar{1}]$, $[\bar{1}1\bar{1}]$, $[\bar{1}\bar{1}1]$), which produce intense optical background signals at low pressure, no longer fluoresce at high pressure and thus increase the ODMR contrast (See supplementary information for details). In conclusion, the observed high contrast is approximately two orders of magnitude higher than previous results at similar pressures^{23,24}.

Secondly, we investigate the effect of inhomogeneous stress on the broadening of the ODMR spectrum (Γ). Together with the ODMR spectrum contrast (C), these two parameters are crucial in determining the sensitivity of magnetic measurements^{25,26}:

$$\eta_B = \frac{4}{3\sqrt{3}} \frac{h}{g_e \mu_B} \frac{\Gamma}{C\sqrt{R}}$$

with the Planck constant h , g-factor g_e , Bohr magneton μ_B and photon-detection rate R .

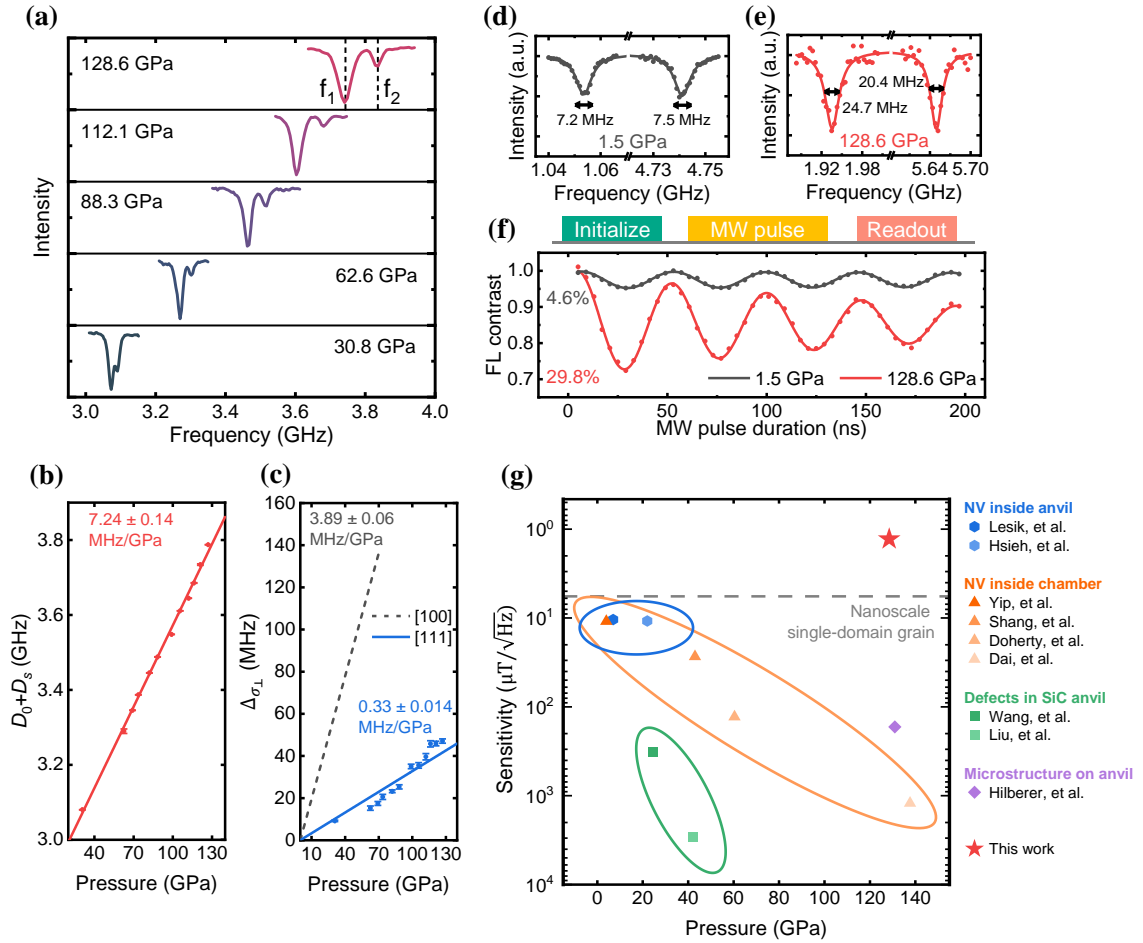


Figure 2. NV centers in crystal orientation designed diamond anvil (a) Zero magnetic field ODMR spectrum of NV centers in pressure, f_1 and f_2 are the resonant frequencies of the left and right peaks in the spectral line respectively, ODMR center frequency $D_0 + D_s = (f_2 + f_1)/2$, and ODMR splitting induced by shear stress $2\Delta\sigma_{\perp} = f_2 - f_1$. (b) Pressure dependence of $D_0 + D_s$. The data are represented by red filled circles with error bars, and the red solid line represents the linear fitting of the data, showing a linear shift of 7.24 MHz/GPa (c) Pressure dependence of $\Delta\sigma_{\perp}$. The blue filled circles with error bars represent the data in (111)-cut anvil, and the blue solid line represents the linear fitting of the data. The dashed grey line represents the result in $\langle 100 \rangle$ -cut anvil by Hilberer et al. showing a linear shift of 0.33 MHz/GPa in (111)-cut anvil and 3.89 MHz/GPa in $\langle 100 \rangle$ -cut anvil²⁴. (d) and (e) The ODMR spectrum linewidth (Γ) tested in ~ 660 Gs magnetic field at 1.5 GPa and 128.6 GPa. The spectrum broadening is about 7 MHz and 20 MHz at the pressure of 1.5 GPa and 128.6 GPa, respectively. (f) Rabi oscillations of NV electron spins. The ODMR contrast is 4.5% and 29.8% at the chamber pressures of 1.5 GPa and 128.6 GPa, shown by gray and red filled circles respectively. The experimental data are fitted by damped sine wave function and plotted by the gray and red solid lines. (g) Comparison of high-pressure magnetometry techniques based on color centers in diamond anvil cell. Our work is marked by red star. The strategy of using NV inside the (100)-cut diamond anvil is marked in blue^{14,15}. The strategy of using NV inside the pressure chamber is marked in orange^{16,17,23,27}. The strategy of fabricating microstructure on anvil is marked

in violet²⁴. The strategy of using the defects in SiC anvil is marked in green^{28,29}. The dashed grey line indicates the magnitude of the remnant magnetic field ($\sim 5.8 \mu\text{T}$) generated by a nanoscale single-domain grain (magnetic moment $10^{-17} \text{ A} \cdot \text{m}^2$, distance 700 nm).

As shown in Fig. 1c, d and Fig. 2b, in the presence of axial stress, the center frequency of $m_s = \pm 1$ spin sublevels shifts from D_0 (2.87 GHz) to $D_0 + D_s$ ^{30,31}. In addition, inhomogeneous axial stress along the NV axis also broadens the ODMR spectrum and reduces the magnetic measurement sensitivity. However, since the stress gradient is mainly perpendicular to the anvil surface and the distribution of the NV centers in z direction is highly concentrated ($\sim 4\text{nm}$ thickness through low-energy (9keV) ion implantation) we can largely suppress the linewidth broadening. As shown in Fig. 2d and e, the linewidth of the ODMR spectrum is narrowed to approximately 20 MHz, a five-fold reduction compared to previous work^{23,24}. With an external magnetic field projected along NV axis (B_z) and shear stress (σ_{\perp}), the energy splitting between $m_s = \pm 1$ sublevels can be expressed as $2\Delta = 2\sqrt{\Delta_B^2 + \Delta_{\sigma_{\perp}}^2}$, determined by the Zeeman splitting ($2\Delta_B = 2\gamma_e B_z$) and the shear stress splitting ($2\Delta_{\sigma_{\perp}}$). In this work, we minimize the shear stress using a (111)-cut anvil and obtain $\Delta \cong \Delta_B$ since $\Delta_B \gg \Delta_{\sigma_{\perp}}$ (Fig. 2c).

As shown in Fig. 2g, the improvement of ODMR contrast and the suppression of spectrum broadening result in a magnetic detection sensitivity of $\sim 1 \mu\text{T}/\sqrt{\text{Hz}}$ at megabar pressure. and the sensor has a sub-microscale spatial resolution due to the combination with a confocal optical detection system (objective NA = 0.4). With such detection sensitivity and resolution, our quantum sensors can investigate the remnant magnetic field generated by nanoscale single-domain grains^{19,20} at megabar pressures.

Magnetic properties investigation at megabar pressures.

Using the quantum sensors, we studied the evolution of the magnetic properties of Fe_3O_4 at pressure from ambient to megabar levels. As the mechanism of the magnetic transition remains unclear, the suppression of the exchange interaction and the spin-orbital coupling is especially complicated in the case of mixed Fe ion valence. Critically, magnetic data on a worldwide mineral collection reveal that pure magnetite which is common in the uppermost mantle and haematite could carry a magnetic remanence down to $\sim 600 \text{ km}^2$ ²¹. The studies on its high-pressure magnetic behaviors are important not only for the fundamental physical and chemical science but also for the understanding of the geomagnetism. Very recently, the single crystal experimental study

on Fe_3O_4 clarified the structure and established the phase diagram at extreme conditions³². This covers three high-pressure phases of Fe_3O_4 : $\alpha\text{-Fe}_3\text{O}_4$ ($Fd\bar{3}m$), $\beta\text{-Fe}_3\text{O}_4$ (Bbmm) and $\gamma\text{-Fe}_3\text{O}_4$ (Pbcm) and the structure changes were related to spin crossover, which have been extensively investigated by neutron scattering, Mossbauer spectroscopy, Fe K-edge X-ray absorption, and magnetic circular dichroism measurements techniques at high pressure^{9,10,33-35}. These experimental results are somewhat contradictory possibly due to the inhomogeneity of the samples such as oxygen vacancies, a variety of stresses induced by different pressure medium, and low resolution of the spectrum at high pressures. Moreover, these experiments studies, which investigate the spin cross over at different Fe sites in the atomic scale, lack experimental observations of the macroscopic magnetism of the samples. A complete understanding of macroscopic effects is almost impossible without knowledge of the underlying domain structure^{36,37}.

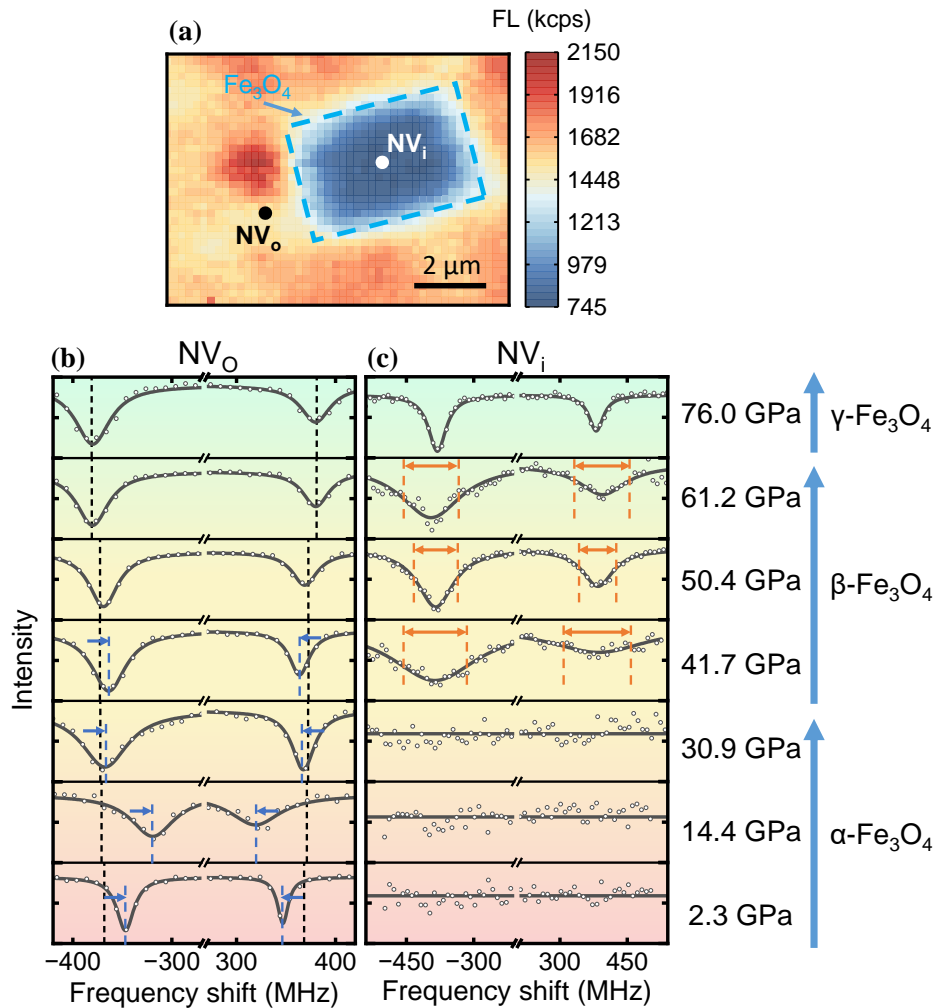


Figure 3. Data for magnetic detection of magnetite (a) Fluorescence (FL) imaging of

NV centers in the anvil tip. Due to the fluorescence resonance energy transfer effect, FL below Fe_3O_4 sample is reduced. The dashed blue square represents the area of Fe_3O_4 sample for eye guide. The filled black and white circle marks the NV centers below the side (NV_o) and beneath (NV_i) the Fe_3O_4 sample, respectively. **(b)** and **(c)** The ODMR spectra of NV_o and NV_i change with elevated pressures, respectively. The horizontal axis represents the frequency shift relevant to the center frequency of $m_s = \pm 1$ spin sublevels. The dashed black lines mark the resonant frequency of the NV centers far away from the sample, which is used to characterize the magnitude of the external magnetic field along NV axis (~ 130 Gs). The dashed blue lines and arrows mark the resonant frequency shift induced by the magnetic field from the sample. The dashed orange lines and arrows mark the spectrum broadening induced by magnetic field fluctuations from the sample.

Here, we carry out the study on the macroscopic magnetism of Fe_3O_4 under megabar pressure. The pressure dependence of magnetic properties is characterized by the ODMR spectra of NV_o and NV_i , as shown in Fig. 3b and c, respectively. The positions of NV_o and NV_i are referred to the Fe_3O_4 sample as illustrated in Fig. 3a.

For NV_o , the static magnetic field induced by magnetite results in additional splitting relative to an external constant bias magnetic field (Fig. 3b). The pressure dependence of the static magnetic field is shown in Fig. 4a, overall revealing a trend of first rising and then falling, and afterwards approaching to 0. From 0-20 GPa, we observe a change in magnetocrystalline anisotropy due to stress. Considering that the external magnetic field is along $\langle 110 \rangle$ of Fe_3O_4 and the initial easy axis is $\langle 111 \rangle$ at ambient pressure, this change in magnetocrystalline anisotropy results in a magnetization enhancement from 0 GPa to 15 GPa. In 20-30 GPa pressure range, magnetic discontinuities and reversals due to drastic changes in magnetic anisotropy are observed, which is close to the first structural phase transition point. After entering the $\beta\text{-Fe}_3\text{O}_4$ phase (30-65 GPa), the magnetic field induced by magnetite gradually degrades, and finally leads to a disappearance of the extra splitting at around 70 GPa.

For NV_i , the magnetic fluctuations on magnetite surface results extra linewidth broadening of ODMR spectra (Fig. 3c). The pressure dependence of the linewidth broadening is shown in Fig. 4b. However, in the $\alpha\text{-Fe}_3\text{O}_4$ phase (0-30 GPa), due to the strong transverse magnetic field $m_s = \pm 1$ and $m_s = 0$ state mixes with each other leading to the disappearance of the ODMR contrast (Fig. 3c)³⁸. As this mixing effect diminishes with the weakening of magnetic field in the $\beta\text{-Fe}_3\text{O}_4$ phase, the expected ODMR is observed but with a strong linewidth broadening due to magnetic fluctuations near the sample. The emergence of magnetic fluctuations implies the existence of intense

frequent movement of the domain walls³⁹, driven thermally or magnetically⁴⁰, or probably stimulated by microwaves or laser light⁴¹. As the pressure increases above 70 GPa, the ODMR broadening caused by magnetic fluctuations disappears (Fig. 4b), implying the disappearance of magnetic domains into the γ -Fe₃O₄ phase, with a high probability associated with the structural phase transition (see supplementary information for phase transition XRD measurement).

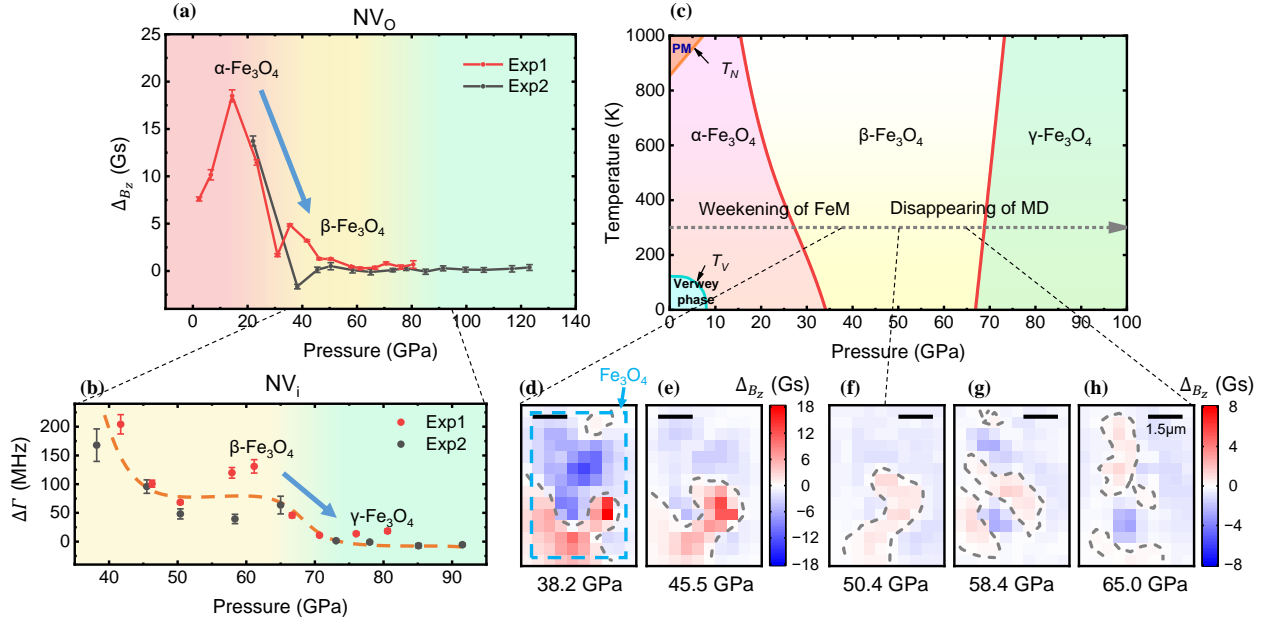


Figure 4. Demagnetization of magnetite to megabar. (a) and (b) Pressure dependence of the extra magnetic field ΔB_z at NV_o and the extra ODMR linewidth $\Delta \Gamma$ of NV_i, respectively. ΔB_z is magnetic field at NV_o minus the external magnetic field. $\Delta \Gamma$ is ODMR spectrum linewidth of NV_o minus the inherent linewidth. The external magnetic field and the inherent linewidth are obtained from the NV centers far away from the sample. The red and black dots with error bars show the experimental results from two DACs with an external magnetic field of ~ 130 Gs and ~ 570 Gs along NV axis respectively. (c) The phase diagram of Fe₃O₄¹⁰. (d) to (h) Magnetic field imaging of the surface of Fe₃O₄ at pressures of 38.2, 45.5, 50.4, 58.4 and 65.0 GPa, respectively. The dashed blue line in (d) marks the Fe₃O₄ sample and dashed gray lines mark the magnetic domain wall.

The magnitude of the static magnetic field (Fig. 4a) and the magnetic fluctuations (Fig. 4b) reveal that, with increasing pressure, the magnetite undergoes a weakening of ferromagnetism (FM) (α -Fe₃O₄ to β -Fe₃O₄) and an eventual loss of ferromagnetism (β -Fe₃O₄ to γ -Fe₃O₄). Imaging the magnetic domains (MD) further enriches the details of this process. In the pressure range of 38 to 50 GPa (Fig. 4d to f), the shape of the MD does not change significantly, but the magnetization intensity decreases, indicating that

the process remains in the ferromagnetic phase and is accompanied by a weakening of the ferromagnetism. In the pressure range of 50 GPa to 70 GPa (Fig. 4f to h), the MD experience a drastic change in shape, implying that the process of MD disappearance begins to occur before the γ -phase transition (70 GPa).

Discussion

Our work extends magnetic measurement technique based on NV centers to the megabar pressure range. Utilizing the improved performance of the quantum sensors, we substantially detect the magnetic properties of single crystal Fe_3O_4 under megabar pressure. Our high spatial resolution magnetic measurement technique can overcome sample inhomogeneities and reveal micro-nanometer scale local magnetism evolution. As demonstrated in our experiment, we observed the evolution of magnetic domains in samples through magnetic imaging.

As illustrated in Fig. 4a, the abrupt drop of Δ_{B_z} above 20 GPa implicates the weakening of magnetism, which means that the spin transition is likely occur in advance of structural transition to $\beta\text{-Fe}_3\text{O}_4$. The Δ_{B_z} at around 40 GPa from two runs of experiments with positive and negative values indicates change in magnetic anisotropy, owing to the magnetic transition related to $\alpha\text{-Fe}_3\text{O}_4$ to $\beta\text{-Fe}_3\text{O}_4$. It is worthy to note that the ferromagnetic phase sustained above 40 GPa and below ~ 420 K was observed by Mossbauer spectroscopy¹⁰. Meanwhile, there is DFT calculations showing that $\beta\text{-Fe}_3\text{O}_4$ (Bbmm) possesses smaller net magnetic moment of $1.7 \mu_B/f.u.$ compared with $4.0 \mu_B/f.u.$ of $\alpha\text{-Fe}_3\text{O}_4$ phase⁴. Our measurements (Fig. 4d to h) do show that very low magnetization in $\beta\text{-Fe}_3\text{O}_4$ but still has magnetic domains, the intensity and shape of domain wall changes above 50.4 GPa (Fig4. f), which might correlate to the onset of magnetic phase transition. This is corresponding to the spin crossover, likely in partial sites of Fe cations, as reported in octahedral sites of Fe^{3+} ³⁴. Furthermore, the disappearance of the magnetic domains in $\gamma\text{-Fe}_3\text{O}_4$ implies a possible entry into non-magnetic state. The possible reason is that only Fe^{3+} ions occupying square antiprism coordinated sites still remain in the HS state (above 84 GPa and down to 2.4 K), which interrupt the magnetic interaction between Fe^{2+} and Fe^{3+} components, suggesting a nonmagnetic state rather than paramagnetic state³⁴. However, the Fe K-edge X-ray absorption and magnetic circular dichroism measurements suggest the loss of the net ordered magnetic moments in $\beta\text{-Fe}_3\text{O}_4$ above 33 GPa, indicating the low spin in three different sites of Fe ions and, thus, a nonmagnetic state⁹. Therefore, in the future work, we expect to combine the variable temperature and magnetic field to obtain the

magnetic P-T phase diagram and saturation magnetization of magnetic materials.

This technique is also applicable to in-situ direct detection of high-temperature superconducting materials under megabar pressure, including various superhydrides compounds^{7,42}. In addition to the DC magnetic field measurements, the optical and spin properties of our NV centers also lift the limitations of nuclear magnetic resonance (NMR) and electron spin resonance (ESR) measurements under megabar pressures. Thus, this work is promising to enabling magnetic resonance imaging (MRI) in pressure chambers thus providing an opportunity to make a great impact generally in investigating high-temperature superconductivity at high pressures^{6,7,43-45}.

Methods

In our experiments, we use a BeCu symmetric diamond anvil cell (Fig. 1a) compressing rhenium gasket to provide a high-pressure environment for Fe₃O₄ samples. A platinum wire is compressed between the gasket and anvil pavilion facets serves as the microwave radiation guide. Nano cBN mixed with epoxy powder isolates the Pt foil and gasket. The sample chamber confined by the gasket and diamond culets is filled with pressure-transmitting medium (PTM) KCl to provide the quasi-hydrostatic environment. The magnetite sample is placed on the diamond surface and compressed together with PTM. Ruby fluorescence (below 20GPa) and Raman spectra of the diamond (above 20 GPa) are used as pressure calibrants⁴⁶.

Diamond anvil we used in experiments are cut and polished from HPHT type-IIas (Non-fluorescent) single crystal diamonds. Both 100 μm and 150μm diameter the culets have been used. The NV centers layer used for magnetic sensing is positioned about ~9 nm deep from the surface of the anvil. The NV centers layer is create by ¹⁴N⁺ ion implantation (Energy: 6 keV Dose: 1*10¹³/cm²) and vacuum annealing treatment (1000°C ~2h). The size of the magnetite sample is about 4 μm *5 μm*1 μm, which is cut from a bulk 99.99% purity single crystal Fe₃O₄ (HeFei Crystal&Surface Technical Material Co., Ltd).

A home-built optical detected magnetic resonance system is used to address NV ensembles inside the DAC and collect fluorescence signal under extreme pressure. (Fig. S1) We use a 532nm laser (CNILaser MGL-III-532-150mW), controlled by two serial acousto-optic modulators (AOM Gooch&Housego AOMO 3200-121), to initialize NV ensembles. The laser beam is focused on the anvil tip through the light port of the DAC using a long working distance objective lens (Mitutoyo MY20X-824, NA0.4), which is

mounted on a piezo scanning stage (Coremorrow P12A.XYZ100S). Through the same objective lens, the NV fluorescence is collected and a dichroic mirror is used to separate it from excitation laser beam. A flip mirror is used to switch the light path between a spectrometer (Horiba iHR550) for pressure measurement and the confocal system, which comprises a 50um pinhole and a 633nm long-pass filter (Semrock BSP01-633R-25). A single photon counting module (Excelitas SPCM-780-24-BR1) is used to collect the fluorescence signal. We use a counter card (National Instruments PCIe-6612) for photon signal counting. A microwave source (Rigol DSG3060) combining a 50W amplifier (Mini-Circuits ZHL-50W-63+) serves to generate MW signal for NV spin manipulation. A Pulse Generator (CIQTEK ASG8100) is used to output pulse sequence and provide timing control for the whole system.

Acknowledgments: The fabrication of diamond sensors was partially performed at the USTC Center for Micro and Nanoscale Research and Fabrication, and the authors particularly thank Dr. Xiaolei Wen, Xiwen Wang, Cunliang Xin, and Hongfang Zuo for their assistance in Fe₃O₄ and sensors fabrication process and Dr. Elena Bykova for her beamtime with X-ray diffraction measurements of Fe₃O₄ at high pressure. This work is supported by the National Natural Science Foundation of China (Grants No. 92265204, 12104447, 12204485), the CAS (GJJSTD20200001), the National Key R&D Program of China (Grants No.2021YFB3202800), the Innovation Program for Quantum Science and Technology (Grant No. 2021ZD0302200), the Anhui Initiative in Quantum Information Technologies (Grant No. AHY050000), the Fundamental Research Funds for the Central Universities.

Author contributions: Jiangfeng Du, Ya Wang and Yu Wang supervised the project, Ya Wang, Yu Wang, and Mengqi Wang proposed the idea of the experiment. Mengqi Wang, and Zhixian Liu built the experimental set-up and performed the measurements. Yu Wang and Ganyu Xu prepared the diamond anvil cell integrated quantum sensor. Mengqi Wang prepared the NV center and the magnetite sample with the help of Pei Yu, Haoyu Sun, and Xiangyu Ye. Bo Yang performed a first-principles calculation. performed the data analysis with contributions from all co-authors. Mengqi Wang, Yu Wang, Zhixian Liu, and Ya Wang performed the data analysis and wrote the manuscript with contributions from all co-authors. All authors contributed to the discussion of the results. All authors discussed the results and commented on the manuscript.

Competing interests: The authors declare that they have no competing interests.

Corresponding author:

Jiangfeng Du(djf@ustc.edu.cn), Ya Wang(ywustc@ustc.edu.cn) and Yu Wang (wangyu@issp.ac.cn)

References

- 1 Mao, H.-K., Chen, X.-J., Ding, Y., Li, B. & Wang, L. Solids, liquids, and gases under high pressure. *Rev. Mod. Phys.* **90**, 015007, doi:10.1103/RevModPhys.90.015007 (2018).
- 2 Diamond, M. R. *et al.* Electron Density Changes across the Pressure-Induced Iron Spin Transition. *Phys. Rev. Lett.* **129**, 025701, doi:10.1103/PhysRevLett.129.025701 (2022).
- 3 Ushakov, A. V., Shorikov, A. O., Anisimov, V. I., Baranov, N. V. & Streltsov, S. V. Suppression of magnetism under pressure in FeS: A DFT+DMFT study. *Phys. Rev. B* **95**, 205116, doi:10.1103/PhysRevB.95.205116 (2017).
- 4 Ju, S., Cai, T.-Y., Lu, H.-S. & Gong, C.-D. Pressure-Induced Crystal Structure and Spin-State Transitions in Magnetite (Fe₃O₄). *J. Am. Chem. Soc.* **134**, 13780-13786, doi:10.1021/ja305167h (2012).
- 5 Streltsov, S. V. & Khomskii, D. I. Covalent bonds against magnetism in transition metal compounds. *Proc. Natl. Acad. Sci.* **113**, 10491-10496, doi:10.1073/pnas.1606367113 (2016).
- 6 Eremets, M. I. *et al.* High-Temperature Superconductivity in Hydrides: Experimental Evidence and Details. *J. Supercond. Novel Magn.* **35**, 965-977, doi:10.1007/s10948-022-06148-1 (2022).
- 7 Errea, I. Superconducting hydrides on a quantum landscape. *J. Phys.: Condens. Matter* **34**, 231501, doi:10.1088/1361-648X/ac5b46 (2022).
- 8 Lilia, B. *et al.* The 2021 room-temperature superconductivity roadmap. *J. Phys.: Condens. Matter* **34**, 183002, doi:10.1088/1361-648X/ac2864 (2022).
- 9 Chen, K. *et al.* Revisiting the Phase Transition of Magnetite under Pressure. *J. Phys. Chem. C* **123**, 21114-21119, doi:10.1021/acs.jpcc.9b04140 (2019).
- 10 Kozlenko, D. P. *et al.* Magnetic and electronic properties of magnetite across the high pressure anomaly. *Sci. Rep.* **9**, 4464, doi:10.1038/s41598-019-41184-3 (2019).
- 11 Troyan, I. *et al.* Observation of superconductivity in hydrogen sulfide from nuclear resonant scattering. *Science* **351**, 1303-1306, doi:doi:10.1126/science.aac8176 (2016).
- 12 Drozdov, A. P., Eremets, M. I., Troyan, I. A., Ksenofontov, V. & Shylin, S. I. Conventional superconductivity at 203 kelvin at high pressures in the sulfur hydride system. *Nature* **525**, 73-76, doi:10.1038/nature14964 (2015).
- 13 Drozdov, A. P. *et al.* Superconductivity at 250 K in lanthanum hydride under high pressures. *Nature* **569**, 528-531, doi:10.1038/s41586-019-1201-8 (2019).
- 14 Hsieh, S. *et al.* Imaging stress and magnetism at high pressures using a nanoscale quantum sensor. *Science* **366**, 1349-1354, doi:doi:10.1126/science.aaw4352 (2019).
- 15 Lesik, M. *et al.* Magnetic measurements on micrometer-sized samples under high pressure using designed NV centers. *Science* **366**, 1359-1362, doi:doi:10.1126/science.aaw4329 (2019).
- 16 Yip, K. Y. *et al.* Measuring magnetic field texture in correlated electron systems under

- extreme conditions. *Science* **366**, 1355-1359, doi:doi:10.1126/science.aaw4278 (2019).
- 17 Doherty, M. W. *et al.* Electronic properties and metrology applications of the diamond NV- center under pressure. *Phys. Rev. Lett.* **112**, 047601, doi:10.1103/PhysRevLett.112.047601 (2014).
- 18 Wang, Z. *et al.* ac Sensing Using Nitrogen-Vacancy Centers in a Diamond Anvil Cell up to 6 GPa. *Phys. Rev. Appl.* **16**, 054014, doi:10.1103/PhysRevApplied.16.054014 (2021).
- 19 Fu, R. R., Lima, E. A., Volk, M. W. R. & Trubko, R. High-Sensitivity Moment Magnetometry With the Quantum Diamond Microscope. *Geochemistry, Geophys. Geosystems* **21**, e2020GC009147, doi:10.1029/2020GC009147 (2020).
- 20 Nagy, L., Williams, W., Tauxe, L., Muxworthy, A. R. & Ferreira, I. Thermomagnetic recording fidelity of nanometer-sized iron and implications for planetary magnetism. *Proc. Natl. Acad. Sci.* **116**, 1984-1991, doi:10.1073/pnas.1810797116 (2019).
- 21 Ferré, E. C., Kuppenko, I., Martín-Hernández, F., Ravat, D. & Sanchez-Valle, C. Magnetic sources in the Earth's mantle. *Nat. Rev. Earth Environ.* **2**, 59-69, doi:10.1038/s43017-020-00107-x (2021).
- 22 Ruoff, A. L., Luo, H. & Vohra, Y. K. The closing diamond anvil optical window in multimegabar research. *J. Appl. Phys.* **69**, 6413-6416, doi:10.1063/1.348845 (1991).
- 23 Dai, J.-H. *et al.* Optically Detected Magnetic Resonance of Diamond Nitrogen-Vacancy Centers under Megabar Pressures. *Chin. Phys. Lett.* **39**, 117601, doi:10.1088/0256-307X/39/11/117601 (2022).
- 24 Hilberer, A. *et al.* NV center magnetometry up to 130 GPa as if at ambient pressure. Preprint at <https://ui.adsabs.harvard.edu/abs/2023arXiv230105094H> (2023).
- 25 Dréau, A. *et al.* Avoiding power broadening in optically detected magnetic resonance of single NV defects for enhanced dc magnetic field sensitivity. *Phys. Rev. B* **84**, 195204, doi:10.1103/PhysRevB.84.195204 (2011).
- 26 Barry, J. F. *et al.* Optical magnetic detection of single-neuron action potentials using quantum defects in diamond. *Proc. Natl. Acad. Sci.* **113**, 14133-14138, doi:10.1073/pnas.1601513113 (2016).
- 27 Shang, Y.-X. *et al.* Magnetic Sensing inside a Diamond Anvil Cell via Nitrogen-Vacancy Center Spins*. *Chin. Phys. Lett.* **36**, 086201, doi:10.1088/0256-307X/36/8/086201 (2019).
- 28 Wang, J.-F. *et al.* Magnetic detection under high pressures using designed silicon vacancy centres in silicon carbide. *Nat. Mater.* **22**, 489-494, doi:10.1038/s41563-023-01477-5 (2023).
- 29 Liu, L. *et al.* Coherent Control and Magnetic Detection of Divacancy Spins in Silicon Carbide at High Pressures. *Nano Lett.* **22**, 9943-9950, doi:10.1021/acs.nanolett.2c03378 (2022).
- 30 Barson, M. S. J. *et al.* Nanomechanical Sensing Using Spins in Diamond. *Nano Lett.* **17**, 1496-1503, doi:10.1021/acs.nanolett.6b04544 (2017).
- 31 Udvarhelyi, P., Shkolnikov, V. O., Gali, A., Burkard, G. & Pályi, A. Spin-strain interaction in nitrogen-vacancy centers in diamond. *Phys. Rev. B* **98**, 075201, doi:10.1103/PhysRevB.98.075201 (2018).
- 32 Khandarkhaeva, S. *et al.* Structural Diversity of Magnetite and Products of Its Decomposition at Extreme Conditions. *Inorg. Chem.* **61**, 1091-1101, doi:10.1021/acs.inorgchem.1c03258 (2022).

- 33 Bengtson, A., Morgan, D. & Becker, U. Spin state of iron in Fe₃O₄ magnetite and h-Fe₃O₄. *Phys. Rev. B* **87**, 155141, doi:10.1103/PhysRevB.87.155141 (2013).
- 34 Greenberg, E. *et al.* High-pressure magnetic, electronic, and structural properties of MFe₂O₄ (M = Mg, Zn, Fe) ferric spinels. *Phys. Rev. B* **95**, 195150, doi:10.1103/PhysRevB.95.195150 (2017).
- 35 Ding, Y. *et al.* Novel Pressure-Induced Magnetic Transition in Magnetite (Fe₃O₄). *Phys. Rev. Lett.* **100**, 045508, doi:10.1103/PhysRevLett.100.045508 (2008).
- 36 Weiss, P. L'hypothèse du champ moléculaire et la propriété ferromagnétique. *J. Phys. Theor. Appl.* **6**, 661-690, doi:10.1051/jphystap:019070060066100 (1907).
- 37 Hubert, A. & Schäfer, R. *Magnetic Domains: The Analysis of Magnetic Microstructures*. (Springer Berlin Heidelberg, 2008).
- 38 Tetienne, J. P. *et al.* Magnetic-field-dependent photodynamics of single NV defects in diamond: an application to qualitative all-optical magnetic imaging. *New J. Phys.* **14**, 103033, doi:10.1088/1367-2630/14/10/103033 (2012).
- 39 Jenkins, A. *et al.* Single-spin sensing of domain-wall structure and dynamics in a thin-film skyrmion host. *Phys. Rev. Mater.* **3**, 083801, doi:10.1103/PhysRevMaterials.3.083801 (2019).
- 40 Kronseder, M. *et al.* Real-time observation of domain fluctuations in a two-dimensional magnetic model system. *Nat. Commun.* **6**, 6832, doi:10.1038/ncomms7832 (2015).
- 41 Tetienne, J.-P. *et al.* Nanoscale imaging and control of domain-wall hopping with a nitrogen-vacancy center microscope. *Science* **344**, 1366-1369, doi:10.1126/science.1250113 (2014).
- 42 Novakovic, L. *et al.* Dispersion interactions in proposed covalent superhydride superconductors. *Phys. Rev. B* **105**, 024512, doi:10.1103/PhysRevB.105.024512 (2022).
- 43 Dasenbrock-Gammon, N. *et al.* Evidence of near-ambient superconductivity in a N-doped lutetium hydride. *Nature* **615**, 244-250, doi:10.1038/s41586-023-05742-0 (2023).
- 44 Ming, X. *et al.* Absence of near-ambient superconductivity in LuH_{2±x}Ny. *Nature*, doi:10.1038/s41586-023-06162-w (2023).
- 45 Meier, T., Petitgirard, S., Khandarkhaeva, S. & Dubrovinsky, L. Observation of nuclear quantum effects and hydrogen bond symmetrisation in high pressure ice. *Nat. Commun.* **9**, 2766, doi:10.1038/s41467-018-05164-x (2018).
- 46 Yuichi, A. & Haruki, K. Pressure calibration of diamond anvil Raman gauge to 410 GPa. *J Phys Conf Ser* **215**, 012195, doi:10.1088/1742-6596/215/1/012195 (2010).